JOURNAL OF AIRCRAFT
Vol. 29, No. 5, Sept.–Oct. 1992

Unsteady Shock-Vortex Interaction on a Flexible Delta Wing

Shigeru Obayashi* and Guru P. Guruswamy†
NASA Ames Research Center, Moffett Field, California 94035

Unsteady Navier-Stokes computations have been carried out for simulating transonic flows over a clipped delta wing undergoing oscillatory and ramp motions, including flexibility. The implicit upwind algorithm has been validated by comparing the solutions with experimental data for the oscillatory pitching motion cases. The numerical and experimental results agree well at moderate angles of attack, where a leading-edge vortex develops. The ramp motion cases have demonstrated the effects of unsteadiness of the flowfield and structural flexibility on the wing responses. For the 10-deg ramp motion, a vortex breakdown is observed. The inviscid interaction with the shock wave plays an essential role in the process of the breakdown observed in the present calculation.

Introduction

IN the last decade, there have been extensive developments in computational fluid dynamics toward the prediction of the three-dimensional flowfield about complex geometries at moderate and high angles of attack. Among the characteristics of flows over aircraft, the behavior of the flow over delta wings is of strong interest for high-speed aircraft because of the nonlinear lift increase due to the leading-edge vortex. Effects of flexibility can further influence the nature of flows on such wings. Steady-state flow problems associated with delta wings have been widely investigated computationally (for example, Refs. 1–3). Several advanced studies have also been performed for unsteady vortical flow calculations at subsonic and supersonic Mach numbers. For example, Ref. 4 presented a conical flow computation on a rigid wing and Ref. 5 presented a subsonic three-dimensional computation on a flexible wing, both involving vortical flows.

Numerical methods can play an important role in complementing expensive wind-tunnel tests, particularly in the area of aeroelasticity. An aeroelastic wind-tunnel experiment is an order of magnitude more expensive than a similar rigid-body experiment involving only aerodynamics. By complementing the experiments with numerical simulations, the overall cost of the development of aircraft can be considerably reduced. Thus development of a numerical method is desired for simulating aeroelastic phenomenon. To accurately compute aeroelastic phenomena it is necessary to solve the unsteady Euler/Navier-Stokes equations simultaneously with the structural equations of motion.

Recently a code, ENSAERO, was developed to compute aeroelastic responses by simultaneously integrating the Euler/Navier-Stokes equations and the modal structural equations of motion using aeroelastically adaptive dynamic grids.[6,7] An upwind algorithm was implemented into the code and the resulting code was successfully applied to compute transonic flows over a typical fighter-type wing undergoing oscillatory motion.[8]

Received March 21, 1991; presented as Paper 90-1109 at the AIAA/ASME/ASCE/AHS/ASC 32nd Structures, Structural Dynamics, and Materials Conference, Baltimore, MD, April 8–10, 1991; revision received Oct. 4, 1991; accepted for publication Oct. 8, 1991.

*Senior Research Scientist, MCAT Institute, San Jose, CA 95127. Member AIAA.

†Research Scientist. Associate Fellow AIAA.

The purpose of this article is to examine the capability of the present numerical method by simulating unsteady transonic flows on a clipped delta wing, which contain a leading-edge separation. So far, unsteady transonic flow computations have dealt with the motion of shock waves on wings only at small angles of attack. The present study focuses on the formation and motion of the leading-edge vortex on a clipped delta wing at transonic speeds as well as motion of the shock wave. The code validation has been done for steady and unsteady pitching cases by comparing surface pressures with the experimental data.[9] Computations for ramp motion cases have demonstrated effects of the unsteadiness of the flowfield and the structural flexibility on the aeroelastic responses.

Governing Aerodynamic Equations and Approximations

The nondimensionalized, thin-layer Navier-Stokes equations used in this study can be written in conservation-law form in a generalized body-conforming curvilinear coordinate system for three dimensions as follows:

$$\partial_\tau \hat{Q} + \partial_\xi \hat{E} + \partial_\eta \hat{F} + \partial_\zeta \hat{G} = \frac{1}{Re}\partial_\zeta \hat{G}^v \tag{1}$$

where $\tau = t$, $\xi = \xi(x,y,z,t)$, $\eta = \eta(x,y,z,t)$, and $\zeta = \zeta(x,y,z,t)$. In the present article, the ξ and η directions are along the streamwise and spanwise directions of a wing, respectively. The viscous derivatives associated with these directions are dropped. In contrast, the ζ direction is normal to the wing surface, and thus the viscous derivatives are retained.

The vector of conserved quantities $\hat{Q}$ and the inviscid flux vector $\hat{F}$ are

$$\hat{Q} = \frac{1}{J}\begin{bmatrix}\rho\\ \rho u\\ \rho v\\ \rho w\\ e\end{bmatrix}, \qquad \hat{F} = \frac{1}{J}\begin{bmatrix}\rho\hat{V}\\ \rho u\hat{V} + \eta_x p\\ \rho v\hat{V} + \eta_y p\\ \rho w\hat{V} + \eta_z p\\ \rho H\hat{V} - \eta_t p\end{bmatrix} \tag{2a}$$

where H is the total enthalpy and $\hat{V}$ is the contravariant velocity component. The time metric is related to the grid velocity as

$$\eta_t = -\eta_x x_t - \eta_y y_t - \eta_z z_t \tag{2b}$$

The Cartesian velocity components u, v, and w are nondimensionalized by the freestream speed of sound a_∞; the density ρ is nondimensionalized by the freestream density ρ_∞; the total energy per unit volume e is nondimensionalized by $\rho_\infty a_\infty^2$. For the ξ and ζ directions, $\hat{E}$ and $\hat{G}$ can be defined similarly.

The viscous flux vector $\hat{G}^v$ is given by

$$\hat{G}^v = \frac{1}{J}\begin{bmatrix} 0 \\ \mu m_1 u_\zeta + \frac{\mu}{3} m_2 \zeta_x \\ \mu m_1 v_\zeta + \frac{\mu}{3} m_2 \zeta_y \\ \mu m_1 w_\zeta + \frac{\mu}{3} m_2 \zeta_z \\ \mu m_1 m_3 + \frac{\mu}{3} m_2(\zeta_x u + \zeta_y v + \zeta_z w) \end{bmatrix} \tag{2c}$$

with

$$\begin{aligned} m_1 &= \zeta_x^2 + \zeta_y^2 + \zeta_z^2 \\ m_2 &= \zeta_x u_\zeta + \zeta_y v_\zeta + \zeta_z w_\zeta \\ m_3 &= \frac{1}{2}(u^2 + v^2 + w^2)_\zeta + \frac{1}{Pr(\gamma - 1)}(a^2)_\zeta \end{aligned} \tag{2d}$$

where Re is the Reynolds number, Pr is the Prandtl number, a is the speed of sound, and J is the transformation Jacobian. Pressure is related to the conservative flow variables $\hat{Q}$ through the equation of state for a perfect gas

$$p = (\gamma - 1)\left\{e - \frac{\rho}{2}(u^2 + v^2 + w^2)\right\} \tag{3}$$

where ρ is the fluid density and e is total energy per unit of volume of the fluid. See Ref. 7 for detailed definitions.

The viscosity coefficient μ in $\hat{G}_v$ is computed as the sum of $\mu_l + \mu_t$ where the laminar viscosity μ_l is taken from the freestream laminar viscosity, assumed to be constant for transonic flows, and the turbulent viscosity μ_t is evaluated by the Baldwin-Lomax algebraic eddy-viscosity model.[10] Since the flowfield to be considered in this article contains a leading-edge separation, it is important to apply the modification of

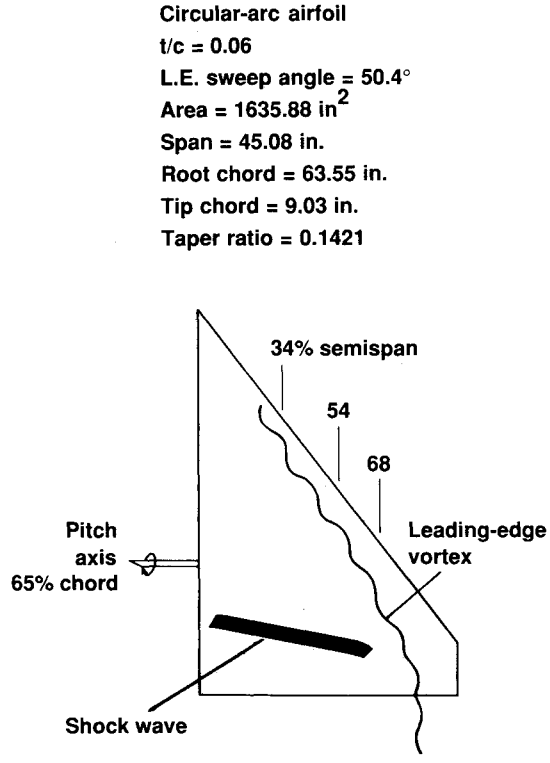

Fig. 1 Planform geometry of clipped delta wing and typical flow structure.

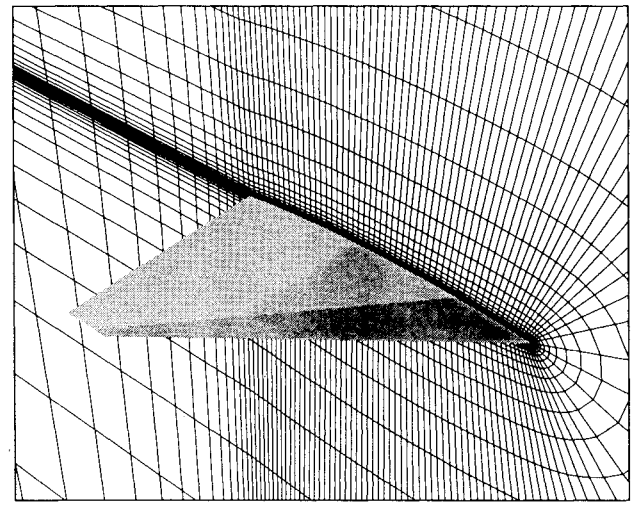

Fig. 2 Clipped delta wing and grid distributions at the root section.

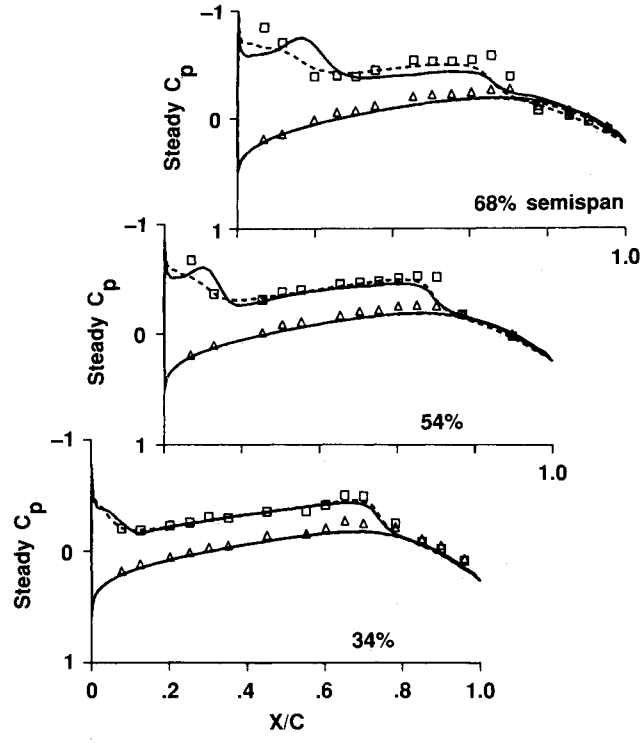

Fig. 3 Comparison of computed steady pressures using the standard and modified Baldwin-Lomax turbulence models with experiment, $M_\infty = 0.90$, $\alpha = 3.97$, $Re_c = 17.6 \times 10^6$. ——, Modified; – – –, unmodified; □, △, experiment, NASA TP-2594.

the turbulence model originally developed for crossflow separation by Degani and Schiff.[11] The modification improves the pressure prediction as shown later, even though the separation is fixed at the sharp leading edge in the following applications.

Although the nature of interaction between vortex and shock wave is predominantly inviscid, the viscous terms are important to compute right vorticity. For example, a test calculation using the Euler equations showed that the leading-edge vortex is weaker because the inviscid model does not resolve the shear layer properly.

Numerical Solution Procedure

Among upwind algorithms, a streamwise upwind algorithm has recently been developed and applied to steady-state problems of transonic flows over wings[12] and vortical flows over a delta wing[13] on fixed grids. Most multidimensional upwind

algorithms are first constructed in one dimension and then extended to multiple dimensions by applying the one-dimensional procedure in each coordinate direction. On the other hand, the present method uses the local stream direction, flow velocity, and pressure gradient to construct the upwinding. The switching of flux evaluations always takes place at sonic values, where transonic shock waves may be located. Therefore, this method follows the flow physics more closely than the coordinate upwind methods. The computed results confirmed the higher resolution of the present algorithm over the central-difference method as well as over other upwind methods.[13] In this work, the streamwise upwind algorithm is applied to compute the inviscid cell-interface fluxes. A second-order central-difference evaluation is applied to the viscous term. The complete algorithm can be found in Refs. 8 and 13.

An implicit method is used for the time integration because the computational efficiency of the method is critical for expensive unsteady viscous calculations. The method chosen here is the LU-ADI (lower-upper factored, alternating direction implicit) method[14] because it requires only scalar bidiagonal matrix inversions. See Refs. 15 and 16 for additional details.

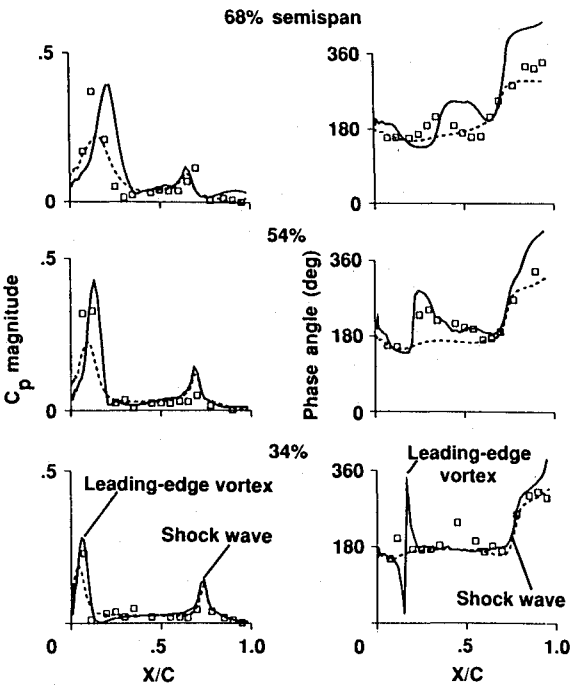

Fig. 4 Comparison of computed unsteady pressures using the standard and modified Baldwin-Lomax turbulence models with experiment, $M_\infty = 0.90$, $\alpha_m = 3.97$, $\bar{\alpha} = 0.46$, $Re_c = 17.6 \times 10^6$, $k = 0.5919$. ——, Modified; – – –, unmodified; □, experiment, NASA TP-2594.

Aeroelastic Equations of Motion

The governing aeroelastic equations of motion of a flexible wing are solved using the Rayleigh-Ritz method. In this method, the resulting aeroelastic displacements at any time are expressed as a function of a finite set of assumed modes. The contribution of each assumed mode to the total motion is derived by Lagrange's equation. Futhermore, it is assumed that the deformation of the continuous wing structure can be represented by deflections at a set of discrete points. This assumption facilitates the use of discrete structural data, such as the modal vector, the modal stiffness matrix, and the modal mass matrix. These can be generated from a finite element analysis or from experimental influence-coefficient measurements. In this study, the finite element method is used to obtain the modal data.

It is assumed that the deformed shape of the wing can be represented by a set of discrete displacements at selected nodes. From the modal analysis, the displacement vector $\{d\}$ can be expressed as

$$\{d\} = [\phi]\{q\} \tag{4}$$

where $[\phi]$ is the modal matrix and $\{q\}$ is the generalized displacement vector. The final matrix form of the aeroelastic

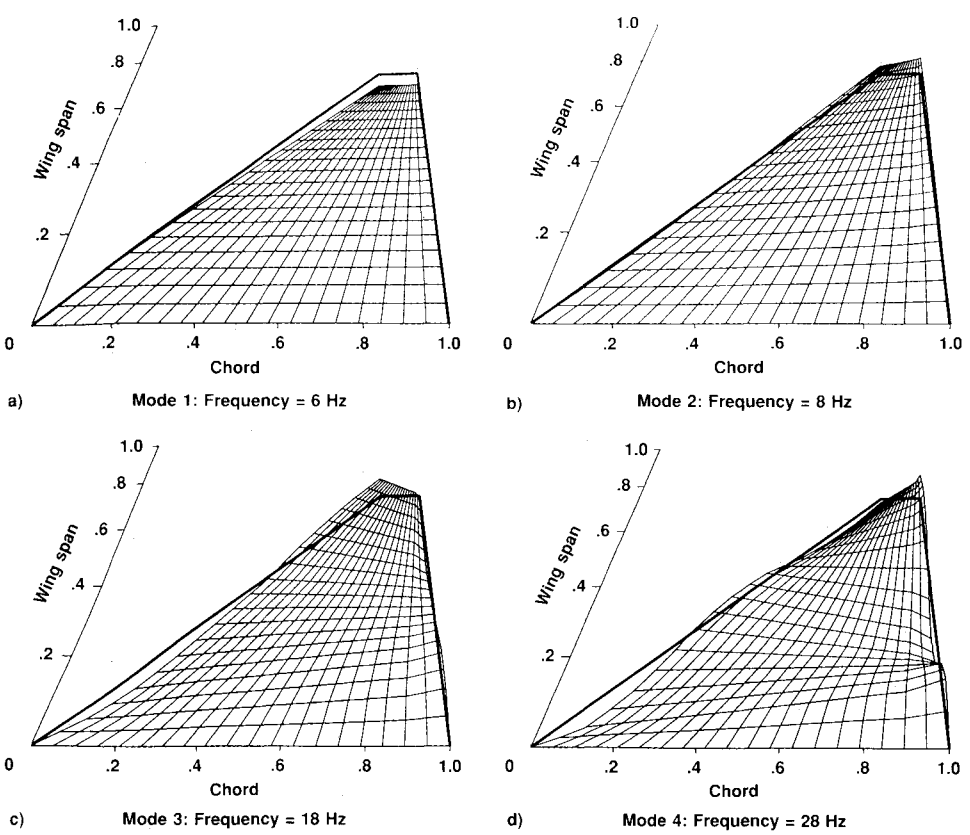

Fig. 5 First four mode shapes and frequencies of clipped delta wing.

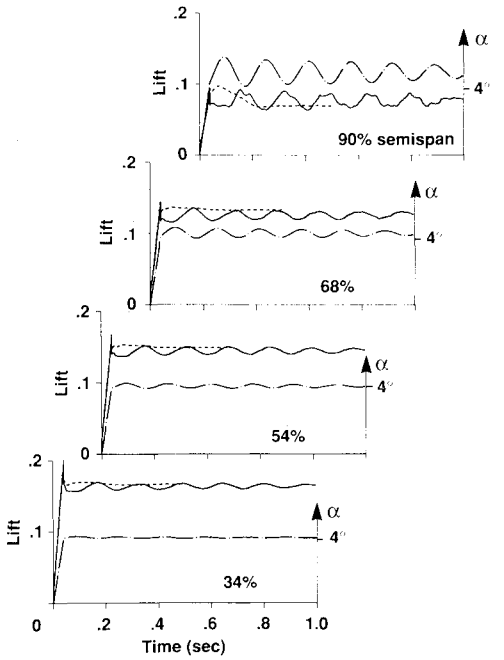

Fig. 6 Comparison of sectional lift responses between rigid and flexible wings in 4-deg ramp motion, $M_\infty = 0.90$, $Re_c = 15.0 \times 10^6$, $A = 0.04$. ——, Flexible; – – –, rigid; —·—, α (rigid + elastic).

equations of motion is

$$[M]\{\ddot{q}\} + [G]\{\dot{q}\} + [K]\{q\} = \{F\} \tag{5}$$

where $[M]$, $[G]$, and $[K]$ are modal mass, damping, and stiffness matrices, respectively. $\{F\}$ is the aerodynamic force vector defined as $(\frac{1}{2})\rho U_\infty^2[\phi]^T[A]\{\Delta C_p\}$ and $[A]$ is the diagonal area matrix of the aerodynamic control points.

The aeroelastic equation of motion [Eq. (5)] is solved by a numerical integration technique based on the linear acceleration method.[17]

Aeroelastic Configuration Adaptive Grids

One of the major deficiencies in computational aerodynamics using the Navier-Stokes equations lies in the area of grid generation. For steady flows, the advance techniques such as zonal grids[18] are being used. Grid generation techniques for aeroelastic calculations, which involve moving components, are in early stages of development. In Ref. 7, aeroelastic configuration adaptive dynamic grids were successfully used for computing time-accurate aeroelastic responses of swept wings. In this work, a similar technique is used.

Results

Numerical schemes used for flow calculations in aeroelasticity must guarantee the correct calculation of amplitude and phase of unsteady pressures. To verify the accuracy of the present code for simulating the complicated flowfield containing a leading-edge vortex and a shock wave, test cases are

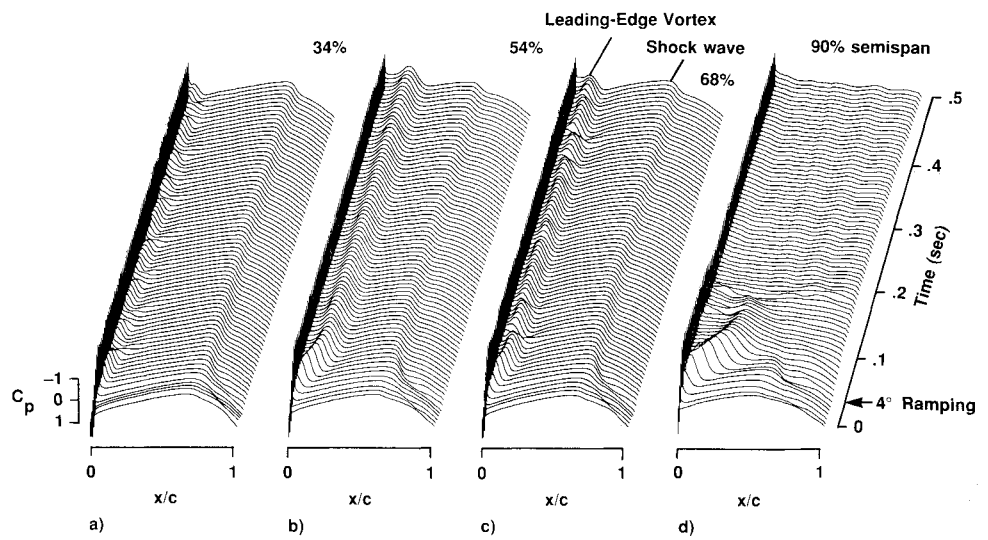

Fig. 7 Unsteady upper surface pressure responses of rigid wing in 4-deg ramp motion, $M_\infty = 0.90$, $Re_c = 15.0 \times 10^6$, $A = 0.04$.

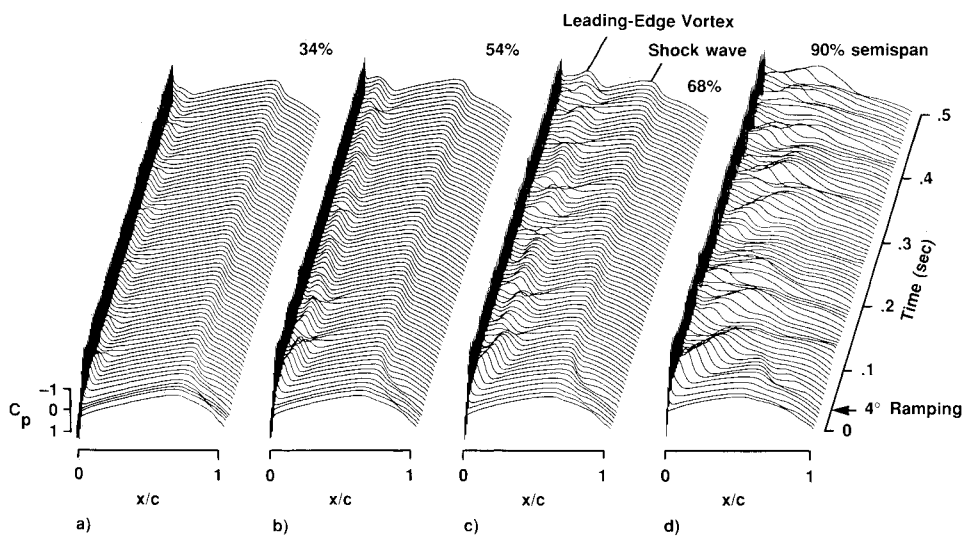

Fig. 8 Unsteady upper surface pressure responses of flexible wing in 4-deg ramp motion, $M_\infty = 0.90$, $Re_c = 15.0 \times 10^6$, $A = 0.04$.

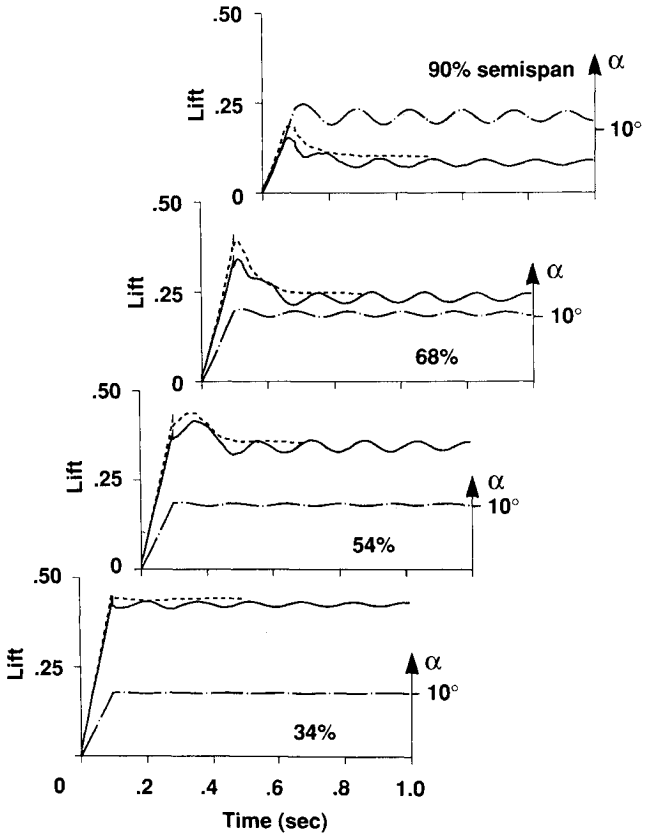

Fig. 9 Comparsion of sectional lift responses between rigid and flexible wings in 10-deg ramp motion, $M_\infty = 0.90$, $Re_c = 15.0 \times 10^6$, $A = 0.04$. ——, Flexible; – – –, rigid; —·—, α (rigid + elastic).

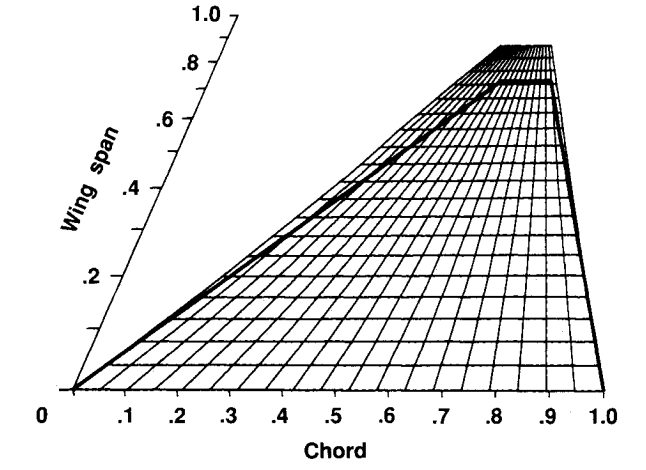

Fig. 10 Deformation of flexible wing at $t \simeq 0.107$ s in 10-deg ramp motion, $M_\infty = 0.90$, $Re_c = 15.0 \times 10^6$, $A = 0.04$.

chosen from the experiment on a clipped delta wing undergoing prescribed pitching motion.[9] Since the experiment was conducted using a Freon test medium, the ratio of specific heats γ is set to 1.135 in the following computations.

Steady Pressures

Steady-state calculations have been performed to examine the validity of the numerical procedure and the computational grid. The model planform geometry is shown in Fig. 1. The wing has a leading-edge sweep angle of 50.4 deg and a 6%-thick circular-arc airfoil section. A typical flow structure is also illustrated in the figure. For this planform with a highly swept leading edge, a strong leading-edge vortex can form at moderate angles of attack. This vortex can interact with a shock wave at transonic Mach numbers. The lines, A, B, and C, indicate the spanwise locations of the pressure orifices in the experiment. Figure 2 shows the grid generated algebraically in the C–H topology. The ξ, η, and ζ coordinates represent the chordwise, spanwise, and normal (to the wing surface) directions, respectively. The grid contains 151 × 25 × 34 points.

The present grid has less number of grid points when compared with the grids used in the typical steady-state computations.[1-3] The number of grid points was determined to compromise the accuracy and the total computational time. Unsteady computations require an order more computational time than the steady-state computations. With the present grid, a typical unsteady case can be computed within 5 h by using a Cray YMP computer with a single processor. (The code requires about 19 μs per grid point per time step for a flexible-wing case.) Then, three different time-step sizes were tried for each case to check the dependency on time-step sizes. Thus, in total, it took about 17 h to complete one unsteady pitching case including the corresponding steady-state computation.

The present grid was chosen from several candidate grids by comparing the pressure distributions computed using each grid with the experiment for a typical flow condition containing both a leading-edge separation and a shock wave at steady state. Among those grids, the H–O grid topology was also considered. However, the results showed that it did not have any advantage over the C–H grid topology either in capturing a leading-edge vortex (because of the moderate sweep angle of the present delta wing) or in capturing a shock wave (because of the relatively coarse grid distribution in the streamwise direction). The present grid is found to give a reasonable agreement with the experiment because the leading-edge vortex is formed at relatively low angles of attack due to the sharp leading edge.

The computed results are shown here for flow conditions at $M_\infty = 0.9$ and $\alpha = 4$ deg. The Reynolds number based on the root chord is about 17 million. Figure 3 shows the comparison of computed steady pressures using the modified and unmodified Baldwin-Lomax turbulence models with the experimental data at 34, 54, and 68% semispan sections. Since the modification accounts for the leading-edge separation, the pressure distribution gives a suction peak due to the leading-edge vortex. In contrast, the unmodified model smears out the vortex so that the suction peak due to the vortex disappears. Thus, the computed results with the modification of the turbulence model successfully capture the flow structures shown by the experimental data.

In the plots, the computed results show good agreement with the experimental data at inboard sections. On the other hand, the comparisons at the outboard section show that the peaks near the leading edge in the computed profiles are located farther downstream than in the experimental data. In other words, the computed results predict the location of the leading-edge vortex more inboard than the experiment. (As a result of the discrepancy in the leading-edge region, the downstream upper-surface pressure shows a minor disagreement, too.)

Since a fine-grid calculation using 151 × 41 × 41 points did not improve the comparison at the leading edge, the source of the discrepancy may be in the computational model rather than the grid resolution. One of the possible sources is the wall effect of the wind tunnel. The present computation assumes a freestream at the far field. Another source is use of a boundary-layer transition strip in the experiment. Even though the modified Baldwin-Lomax model is used here, the computation assumes a fully turbulent flow. The other possible source is the geometry definition at the tip. The report[9] does not have enough information to represent a detailed wing tip shape. In addition, the grid represents a clean wing, whereas the experimental model has some surface irregularities because of control surfaces both at the leading edge and at the trailing edge.

In Ref. 19, four steady-state cases are computed for flow conditions at $M_\infty = 0.88$ and 0.9 with angles of attack $\alpha = 3$ and 4 deg. The experimental data do not show the presence of a shock wave at $M_\infty = 0.88$. With an increase of the Mach number from 0.88 to 0.9, a shock wave is formed on the upper surface of the wing. On the other hand, an increase in the angle of attack from 3 to 4 deg at a fixed Mach number primarily affects the strength of the leading-edge vortex. The computed results successfully represent the effects of the different Mach numbers and the different angles of attack.

Rigid Pitching Motion

The unsteady data are given for the case when the rigid wing is oscillating in a pitching mode, $\alpha(t) = \alpha_m - \bar{\alpha}\sin(\omega t)$, about an axis at 65.22% root chord, where ω is the circular frequency in radians per second. The test cases consider four flow conditions at $M_\infty = 0.88$ and 0.9 with mean angles of attack $\alpha_m = 3$ and 4 deg, a pitch amplitude $\bar{\alpha} = 0.5$ deg, and a frequency of 8 Hz that corresponds to a reduced frequency of $k \simeq 0.6$ ($k = \omega c/U_\infty$ where c is the root chord).

Unsteady computations are started from the corresponding steady-state solutions. The number of time steps per cycle of 3600 was chosen from the numerical experiments to assure the time accuracy (the typical time-step size was about 3.3×10^{-3}). The convergence of the unsteady computations to a periodic flow is verified by comparing the results between cycles. The third-cycle results are shown in the following. The numerical transient is confirmed to disappear within two cycles.

Figure 4 shows the comparison of computed unsteady pressures using the modified and unmodified Baldwin-Lomax turbulence models with the experimental data at $M_\infty = 0.9$ and $\alpha_m = 4$ deg, corresponding to Fig. 3. The plots show the comparison of the magnitude and phase angle between the computed and measured unsteady upper surface pressure coefficients of the wing at 34, 54, and 68% semispan sections. Both the leading-edge vortex and the shock wave produce a peak in magnitude and a jump in phase angle. Since the unmodified model gave almost two orders of magnitude higher turbulent viscosity at the leading edge, the solution became highly dissipative and thus did not show any large changes in unsteady pressures. (In Fig. 4a, the modified turbulence model predicts a larger phase change than the experiment near $x/c = 0.15$. This is partly due to the conversion of unsteady pressures from real and imaginary to magnitude and phase angle.) The improvements due to the modification of the turbulence model are seen in both magnitude and phase angle where the leading-edge vortex exists. Consistent to the steady pressures, the peaks near the leading edge in the computed profiles are located more downstream than the experimental data at the outboard sections. Overall, the numerical results show fairly good agreement with the experimental data. The present grid leads to reasonable resolution for the present unsteady flowfields, even though the grid is fairly coarse.

Throughout the four test cases presented in Ref. 19, the modified turbulence model predicted higher peaks in magnitude and larger changes in the phase angle at the leading-edge vortex and thus agreed with the experiment better than the unmodified model. The effect of Mach numbers on the shock wave and the effect of angles of attack on the vortex were consistent to the steady-state results.

Rigid and Flexible Ramp Motions

In maneuvering, aircraft often undergo rapid ramp motions. During such motions, flow unsteadiness and wing flexibility play important roles. In this section, the applicability of the present development to computing such flowfields is demonstrated.

Computations are performed for rigid and flexible wings in ramp motion. Structural properties of the wing were selected to represent a typical fighter wing. Figure 5 shows the mode shapes and the frequencies of the first four normal modes for the clipped delta wing used in the following computations. The dynamic pressure is set to be 1.0 psi. Test cases consider 4- and 10-deg ramp motions from 0-deg angle of attack for both rigid and flexible wings.

4-Deg Ramp Motion

Figure 6 shows the comparisons of the sectional lift responses between the rigid and flexible wings at $M_\infty = 0.9$ and $Re_c = 15 \times 10^6$ for the wing ramping up to 4 deg with a pitch rate of $A = 0.04$. The pitch rate A is defined as $\dot{\alpha}c/U_\infty$. The variation of the effective angle of attack including both the ramp angle and the flexible angle of attack is also shown for the flexible-wing case. The data are plotted at 34, 54, 68, and 90% semispan sections. The unsteady computations are started from the converged steady-state solution at 0-deg angle of attack.

In the rigid-wing case, the lift responses at the inboard sections settle down quickly after the ramp motion stops, and the flow approaches the steady-state values. (Thus the com-

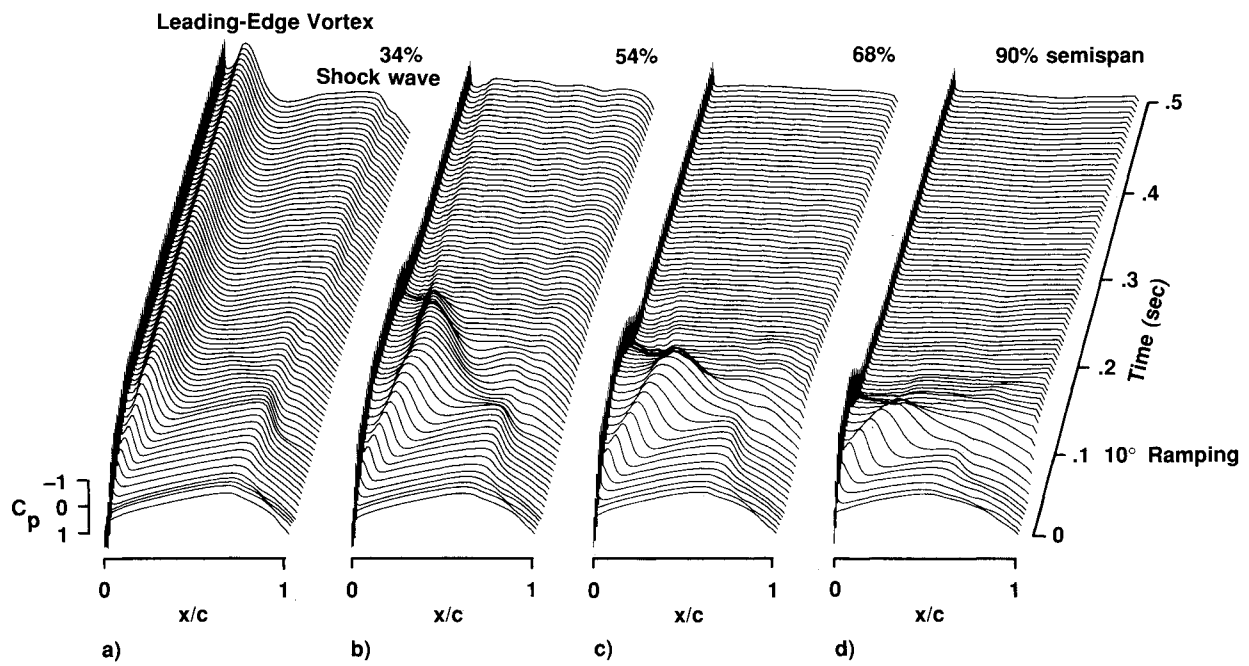

Fig. 11 Unsteady upper surface pressure responses of flexible wing in 10-deg ramp motion, $M_\infty = 0.90$, $Re_c = 15.0 \times 10^6$, $A = 0.04$.

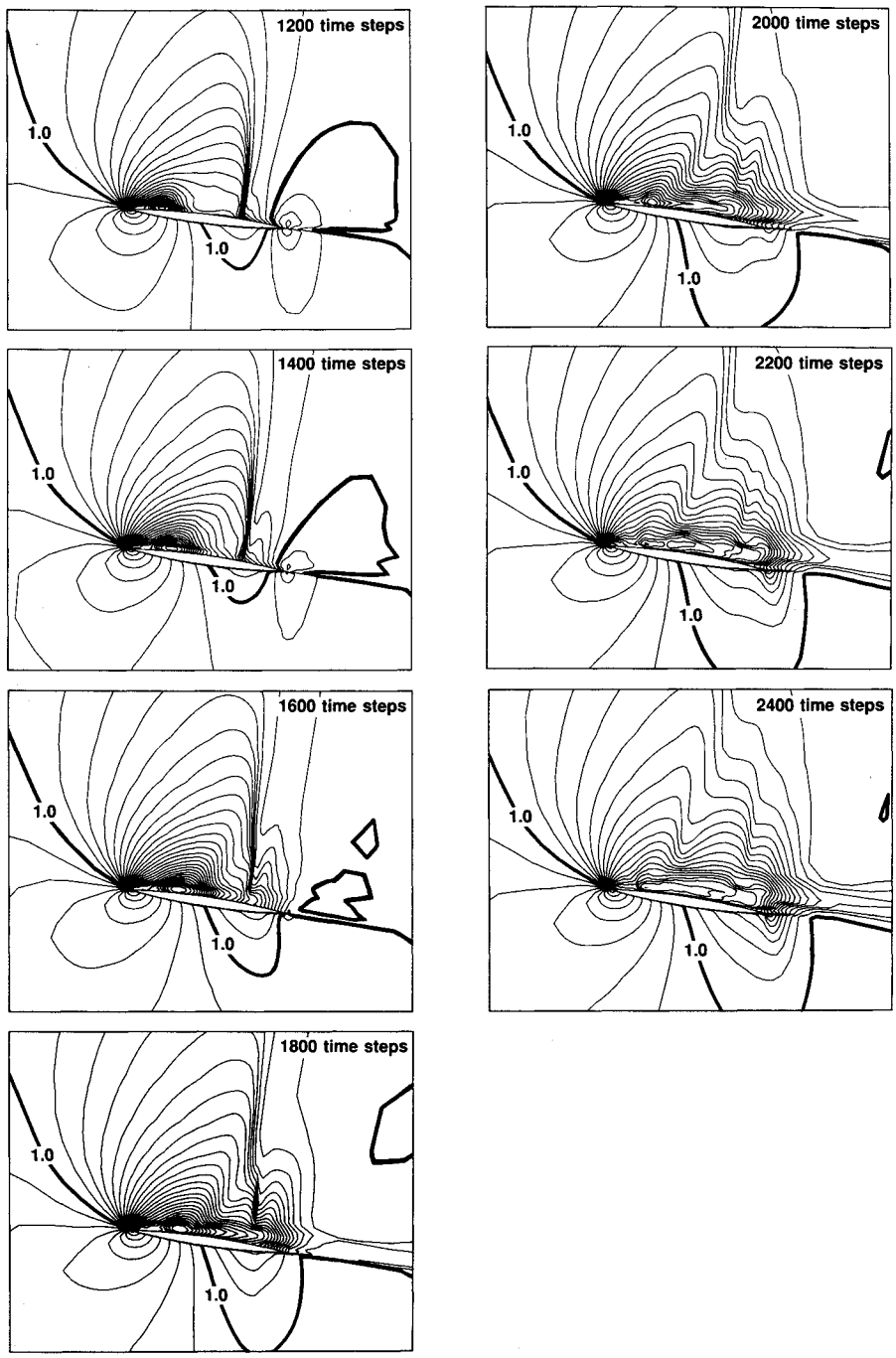

Fig. 12 Instantaneous density contour plots at 68% semispan section in 10-deg ramp motion ($0.08 < t < 0.16$ s), $M_\infty = 0.90$, $Re_c = 15.0 \times 10^6$, $A = 0.04$.

putation was stopped at $t \simeq 0.5$ s.) At the 90% section, however, the lift continues to increase for a short period after the ramp motion stops. This corresponds to the movement of the leading-edge vortex as indicated in the corresponding pressure history shown in Fig. 7. In Fig. 7, the pressure distributions are plotted every 100 time steps. The ramp motion ends at 600 time steps ($t = 0.04$ s), which corresponds to the sixth plot from the bottom. At the 90% section in Fig. 7d, a leading-edge vortex is formed and lifts off from the wing surface. This results in the increase and then a decrease of the sectional lift shown in Fig. 6. At the other inboard sections in Fig. 7, the pressure distributions become similar to those in Fig. 3, i.e., the leading-edge vortex remains without interacting with the shock wave. Thus, the corresponding sectional lift stays nearly steady with minor fluctuations due to the movement of the vortex, as seen in Fig. 7a.

In contrast to the rigid-wing case, Fig. 6 shows that the sectional lift responses of the flexible wing are oscillatory. The primary oscillation is about 6 Hz, which corresponds to the frequency of the first mode. As the wing moves downward, the lift increases, and vice versa. The overall oscillation is damping. The first mode response is damping, but the second mode response stays oscillatory.[19] The primary effect of the flexibility is the reduction of the lift at most of the spanwise sections due to the reduced angles of attack. Figure 8 shows the corresponding pressure history plots. The plots in Figs. 8c and 8d show the shedding of the leading-edge vortex in comparison to the plots of the rigid wing in Figs. 7c and 7d. In addition, Fig. 6 shows that the 90% sectional lift response of the flexible wing has the low-frequency primary oscillation perturbed by a high-frequency vortex shedding. The low-frequency primary oscillation (6 Hz) corresponds to the structural oscillation. The high-frequency perturbation corresponds to the shedding of the vortex that can be seen in the pressure plots of Fig. 8d. This frequency (about 15 Hz) does not excite any structural mode as shown in Fig. 5.

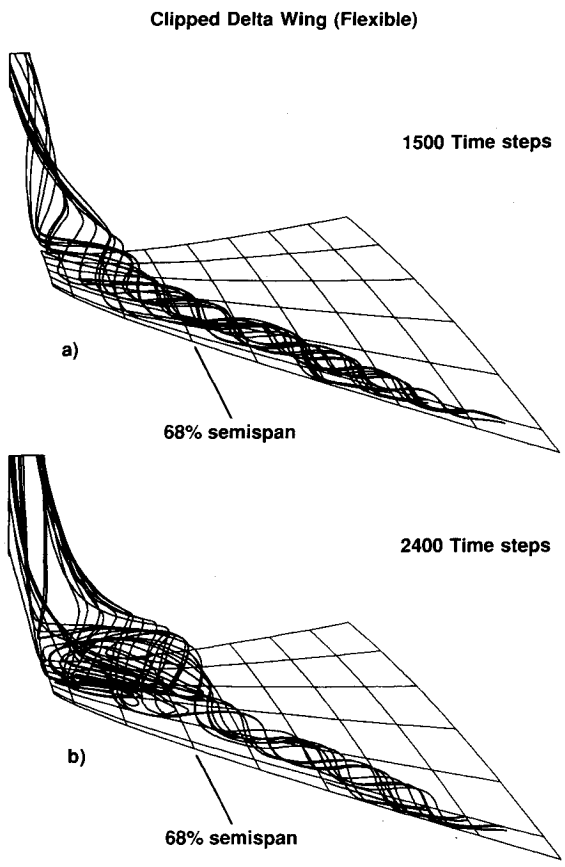

Fig. 13 Streamline pattern over the upper surface of flexible wing in 10-deg ramp motion, $M_\infty = 0.90$, $Re_c = 15.0 \times 10^6$, $A = 0.04$. a) $t = 0.10$ s, and b) $t = 0.16$ s.

Computations (not shown) were also carried out for the flexible-wing ramping from 0 to 3 deg and from 0 to 5 deg at the same pitch rate as the 4-deg case. The 4-deg case shows the largest high-frequency perturbation. In the 3-deg case, the vortex is not strong enough to disturb the lift response. The vortex shedding is found only at the 90% section. In the 5-deg case, the vortex lifts off from the wing surface so that the structural oscillation does not cause the perturbation seen at the lower angles of attack. The 10-deg case discussed in the next section does not show the perturbation either.

A reduction of the local angle of attack due to the flexibility of the wing results in a delay of the lift increase for a short period after the ramp motion stops (about $0.04 < t < 0.11$ in Fig. 6). The wing is deformed upward in bending and leading-edge down in twisting. When the ramp motion stops, the wing is still deforming, which also gives a dynamic effect. Thus the local angle of attack relative to the wing section decreases toward the wing tip and the leading-edge vortex appears weaker in the flexible-wing case. This leads to the delay of the lift increase in the flexible-wing case.

10-Deg Ramp Motion

The sectional lift responses for the 10-deg ramp motion at several spanwise sections are shown in Fig. 9. The computations are again started from the steady-state solution at 0-deg angle of attack. The unsteady increase of the lift is observed more widely in both rigid and flexible cases than the 4-deg case. The sectional lift at the 90% section indicates a stall before reaching 10-deg angle of attack for both rigid and flexible wings. Instead, the plot does not have any significant perturbations. The flexible wing gives lower lift because of the deformation of the wing similar to the 4-deg case. After the initial lift increase, the lift oscillates due to the structural oscillation. Again, the first mode response is damping, but the second mode response stays oscillatory.[19] Figure 10 shows the magnified deformation of the wing at 1600 time steps (the ramp motion ends at 1500 time steps: $t = 0.10$ s). The actual displacement of the leading edge at the wing tip is 1.7% of the root chord length.

Figure 11 shows the corresponding pressure history plots of every 100 time steps for the flexible-wing case. In contrast to the 4-deg case, the deformation of the wing does not affect the flowfield as strongly because the leading-edge vortex lifts off from the wing surface at the outboard sections. The flexibility does not play an important role at the inboard sections, because the wing root is fixed. Thus there is no significant difference in the responses between the rigid and flexible wings. At the most inboard section in Fig. 11, the pressure distributions show no interaction of the leading-edge vortex with the shock wave. At the 54% section, both vortex and shock wave develop, then both disappear. At the 68% section, a similar but more rapid change occurs. This rapid reduction of the lift indicates a vortex breakdown.

To see the interaction of the leading-edge vortex with the shock wave, the density contours at the 68% section are plotted every 200 time steps from 1200 to 2400 time steps ($0.08 < t < 0.16$) in Fig. 12. First, there is no interaction between the vortex and the shock wave. As the vortex develops, it moves toward the trailing edge, that is, toward the shock wave. When the vortex starts to interact with the shock wave, the shock wave starts to ride on the shear layer and to form a lambda-type shock wave. At this point, the shock wave disappears from the surface pressure plots. As the front shock grows, the flow separation grows and the vortex core bursts quickly. Simultaneously, the rear shock weakens. Finally, the fully separated flow is observed. The corresponding contour plots of the negative u component in Ref. 19 show that a negative u region appears as the vortex is deformed by the strong front shock at 2000 time steps ($t \simeq 0.13$ s). As the vortex core diffuses, the reverse flow region grows. The shock wave plays an essential role in the process of this breakdown.

Figure 13 shows plots of the streamline pattern at 1500 and 2400 time steps ($t = 0.10, 0.16$ s, respectively). At 1500 time steps, when the ramp motion has just ended, a leading-edge separation is formed over the entire span. Although it is not clear from the plots, the vortex starts bursting near the tip as indicated in Fig. 11d. In contrast, at 2400 time steps, a bubble-type breakdown is clearly observed in the middle of the span. The breakdown grows toward the upstream slowly. Then the flow reaches the nearly steady state.

Although no corresponding experiment was performed for the present wing at this angle of attack, Ref. 20 reported a vortex breakdown about a similar wing at similar flow conditions, including a comparison with the experiment.

Concluding Remarks

In this paper, a computational procedure for computing the unsteady transonic flows associated with the leading-edge vortex on a clipped delta wing, including flexibility, has been presented. The procedure is based on a time-accurate computational method combined with the use of aeroelastically adaptive dynamic grids. The flow is modeled using the Navier-Stokes equations. The flow equations are coupled with the structural equations to account for the flexibility. The numerical procedure has been verified through the comparisons with the experiment for the unsteady pitching cases on the rigid clipped delta wing. The main flow structures are successfully captured.

The ramp motion cases have demonstrated the effects of unsteadiness of the flow field and flexibility of the wing. The primary effect of the flexibility is the reduction of the lift due to the deformation of the wing. Interaction of the leading-edge vortex with the shock wave has significant effects on the wing responses. For the 4-deg ramp motion, the vortex shedding occurs at the wing tip due to the flexibility. For the 10-deg ramp motion, a possible vortex breakdown is observed. The inviscid interaction with the shock wave plays an essential

role in the process of the breakdown observed in the present calculation.

References

[1]Fujii, K., and Schiff, L. B., "Numerical Simulation of Vortical Flows over a Strake-Delta Wing," *AIAA Journal*, Vol. 27, No. 9, 1990, pp. 1153–1162.

[2]Taylor, S. L., Kjelgaard, S. O., Weston, R. P., Thomas, J. L., and Sellers, W. L., III, "Experimental and Computational Study of the Subsonic Flow About a 75° Swept Delta Wing," AIAA Paper 87-2425, Aug. 1987.

[3]Ekaterinaris, J. A., and Schiff, L. B., "Numerical Simulation of the Effects of Variation of Angle of Attack and Sweep Angle on Vortex Breakdown over Delta Wings," AIAA Paper 90-3000-CP, Aug. 1990.

[4]Kandil, O. A., and Chuang, H. A., "Computation of Vortex-Dominated Flow for a Delta Wing Undergoing Pitching Oscillation," *AIAA Journal*, Vol. 28, No. 9, 1990, pp. 1589–1595.

[5]Guruswamy, G. P., "Vortical Flow Computations on Swept Flexible Wings Using Navier-Stokes Equations," AIAA Paper 89-1183, April 1989.

[6]Guruswamy, G. P., "Unsteady Aerodynamic and Aeroelastic Calculations of Wings Using Euler Equations," *AIAA Journal*, Vol. 28, No. 3, 1990, pp. 461–469.

[7]Guruswamy, G. P., "Navier-Stokes Computations on Swept-Tapered Wings, Including Flexibility," AIAA Paper 90-1152, April 1990.

[8]Obayashi, S., Guruswamy, G. P., and Goorjian, P. M., "Application of a Streamwise Upwind Algorithm for Unsteady Transonic Computations over Oscillating Wings," AIAA Paper 90-3103, Aug. 1990.

[9]Hess, R. W., Cazier, F. W., Jr., and Wynne, E. C., "Steady and Unsteady Transonic Pressure Measurements on a Clipped Delta Wing for Pitching and Control-Surface Oscillations," NASA TP-2594, Oct. 1986.

[10]Baldwin, B. S., and Lomax, H., "Thin-Layer Approximation and Algebraic Model for Separated Turbulent Flows," AIAA Paper 78-257, Jan. 1978.

[11]Degani, D., and Schiff, L. B., "Computations of Turbulence Supersonic Flows Around Pointed Bodies Having Crossflow Separation," *Journal of Computational Physics*, Vol. 66, No. 1, 1986, pp. 173–196.

[12]Goorjian, P. M., "A New Algorithm for the Navier-Stokes Equations Applied to Transonic Flows Over Wing," AIAA Paper 87-1121-CP, June 1987.

[13]Obayashi, S., and Goorjian, P. M., "Improvements and Applications of a Streamwise Upwind Algorithm," AIAA Paper 89-1957-CP, June 1989.

[14]Obayashi, S., "Numerical Simulation of Underexpanded Plumes Using Upwind Algorithms," AIAA Paper 88-4360-CP, Aug. 1988.

[15]Obayashi, S., Goorjian, P. M., and Guruswamy, G. P., "Extension of a Streamwise Upwind Algorithm to a Moving Grid System," NASA TM-102800, April 1990.

[16]Obayashi, S., Matsushima, K., Fujii, K., and Kuwahara, K., "Improvements in Efficiency and Reliability for Navier-Stokes Computations Using the LU-ADI Factorization Algorithm," AIAA Paper 86-0338, Jan. 1986.

[17]Guruswamy, P., and Yang, T. Y., "Aeroelastic Time Response Analysis of Thin Airfoils by Transonic Code LTRAN2," *Computers and Fluids*, Vol. 9, No. 4, 1980, pp. 409–425.

[18]Flores, J. "Simulation of Transonic Viscous Wing and Wing-Fuselage Flows Using Zonal Methods," NASA TM-89421, March 1987.

[19]Obayashi, S., and Guruswamy, G. P., "Unsteady Shock-Vortex Interaction on a Flexible Delta Wing," AIAA Paper 91-1109, April 1991.

[20]Tu, E. L., "Navier-Stokes Simulation of a Close-Coupled Canard-Wing-Body Configuration," AIAA Paper 91-0070, Jan. 1991.